Rare Met. (2023) 42(5):1508–1515
https://doi.org/10.1007/s12598-022-02208-6

RARE METALS

ORIGINAL ARTICLE

Surface amorphization oxygen vacancy-rich porous Sn_3O_x nanosheets for boosted photoelectrocatalytic bacterial inactivation

Long-Wei Wang, Lin Liu, Zhen You, Li-Wei Zhang, Xiao-Di Zhang, Na Ren, Hong Liu*, Xin Yu*

Received: 22 July 2022 / Revised: 19 August 2022 / Accepted: 7 September 2022 / Published online: 10 February 2023
© Youke Publishing Co., Ltd. 2023

Abstract Antibiotic misuse has resulted in the emergence of superbugs, warranting new antibacterial methods. Surface amorphisation oxygen vacancy-rich porous Sn_3O_x nanosheets in situ grown on Ni foam are successfully designed via a simple, one-step hydrothermal method, resulting in enhanced photoelectrochemical (PEC) bacterial inactivation. In this system, the porous structure enriches its surface with oxygen vacancies, which can extend the absorption spectrum into the near-infrared region, while oxygen vacancies can enhance the separation of electron–hole pairs. Most importantly, the sheet-like porous structure enhances surface active sites and increase the contact area between bacteria and electrodes. Therefore, the reactive oxygen species produced during the PEC process can directly act on the surface of bacteria and is 100% effectively against drug-resistant Gram-positive and Gram-negative bacteria in water within 30 min. This study acts as a foundation for the development of novel photoelectrocatalyst electrodes for efficient water purification.

Keywords Oxygen vacancy; Photoelectrocatalysis; Water purification; Sn_3O_x; Bacterial killing

Long-Wei Wang and Lin Liu have contributed equally to this work.

Supplementary Information The online version contains supplementary material available at https://doi.org/10.1007/s12598-022-02208-6.

L.-W. Wang, L. Liu, L.-W. Zhang, N. Ren, H. Liu*, X. Yu*
Institute for Advanced Interdisciplinary Research (iAIR), School of Chemistry and Chemical Engineering, University of Jinan, Jinan 250022, China
e-mail: hongliu@sdu.edu.cn

X. Yu
e-mail: ifc_yux@ujn.edu.cn

L.-W. Wang, Z. You
Key Laboratory of Resource Biology and Biotechnology in Western China, Ministry of Education School of Medicine, Northwest University, Xi'an 710069, China

X.-D. Zhang
Institute for Cell Engineering, Department of Neurology, Johns Hopkins University School of Medicine, Baltimore, MD 21205, USA

H. Liu
State Key Laboratory of Crystal Material, Shandong University, Jinan 250100, China

1 Introduction

Global antimicrobial drug abuse currently is an extremely serious issue, with "superbug" infections killing at least 700,000 people annually [1, 2]. The number of deaths is expected to increase to 10 million per year by 2050 [3, 4]. Various disinfection techniques, such as ultraviolet (UV) irradiation [5], ozonation [6], and chlorination [7], have been widely used to inactivate drug-resistant bacteria. However, those disinfection techniques consume large amounts of chemicals, producing harmful by-products, and are energy-intensive, contributing to climate change [8–11]. Furthermore, since most drug-resistant bacteria live in water, their inactivation is challenging [12, 13]. It is critical to develop new antibacterial agents that can effectively kill drug-resistant bacteria in water without causing antibiotic resistance, ensuring safe drinking water.

Photocatalytic purification has recently garnered significant attention because of its environmental friendliness, safety, excellent stability, and high reusability [14–18]. Reactive oxygen species (ROS), which can be generated on a

photocatalyst exposed to light, can effectively kill bacteria [19–22]. Most importantly, solar light is the most abundant free renewable energy source that can be used as the light source for the photocatalytic system [23, 24]. A large number of photocatalysis, including TiO_2, have been discovered, and present an economical, effective, and environmentally friendly oxidation process for purification [25–28]. Furthermore, these inorganic nanomaterial antibacterial agents would not cause bacteria to develop drug resistance [29–31]. Because of the large band gap (approximately 3.20 eV), conventional TiO_2 can only absorb ultraviolet (UV) light and is therefore inactive in the visible spectral range, with bactericidal efficiency far from optimal for real-world applications [32–34]. Furthermore, nanomaterials are difficult to recycle and are bound to cause secondary pollution when used for water purification [35–37].

The photoelectric approach successfully bridges the gap in current photocatalysis and provides a multitude of potential advantages: (1) Quick electron transport via direct contact between the substrate electrode and photocatalytic active material [38, 39]. (2) A large number of photocatalytically active sites to assure high photoelectric conversion efficiency [40, 41]. (3) The photoelectric catalytic electrode is simple to remove from the solution, produces no secondary pollution, and can be reused [42, 43].

Recent studies have demonstrated photoelectrocatalytic application in the environment and energy fields [44–46]. Zhang and colleagues [47] successfully grew MoS_2/MoO_x on the Ti film electrodes, demonstrating excellent bacterial inactivation activity (the bacteria inactivation efficiency of *Escherichia coli* (*E. coli*) reached 99.9999% in 2 h). Ye and colleagues reported the development of a three-dimensional (3D) lupine-like TiO_2/Sn_3O_4 heterostructure photoanode with a high water-splitting performance [48]. According to previous research, a Sn_3O_4/Ni foam photoanode was synthesised via enhanced photoelectrocatalytic degradation of polyacrylamide. Sn_3O_4 is an oxide with a layered structure of mixed valence Sn^{2+} and Sn^{4+} and a band gap of approximately 2.8 eV [49]. It has been established that Sn_3O_4 can harvest visible light and use it to catalyse the organic degradation of various compounds [50]. Thus, Sn_3O_4 may exhibit a higher potential for photoelectrocatalytic bacterial inactivation than TiO_2.

In this study, surface amorphisation oxygen vacancy-rich porous Sn_3O_x nanosheets were grown on Ni foam using a simple, one-step hydrothermal method, resulting in enhanced photoelectrochemical (PEC) bacterial inactivation properties. This method is simple, convenient, and safe when compared to the traditional H_2 post-processing method for generating oxygen vacancies. With the enhancement of the PEC performance, the photo anode killed bacteria with an antibacterial efficiency of up to 100% in 30 min.

2 Results and discussion

Firstly, the Sn_3O_4 nanosheets were grown in situ on Ni foam surfaces using a hydrothermal method similar to our previous research [51]. During the nucleation of Sn_3O_4, ascorbic acid was added to obtain an oxygen vacancy-rich Sn_3O_4. Ascorbic acid with reducing properties an adsorb oxygen atoms and increases the oxygen vacancy concentration of the material. To facilitate the distinction, we referred to the Sn_3O_4 that was mixed with ascorbic acid during the preparation process as Sn_3O_x. Scanning electron microscopy (SEM) and transmission electron microscopy (TEM) were used to examine the morphologies and structural characteristics of the samples. Figure S1a shows a clear 3D network structure of the Ni foam, with the branches interlacing to form pores of varying sizes. The Ni foam has a smooth surface (Fig. S1b). 3D foam-like network structure is still present growing Sn_3O_4 on the surface (Fig. 1a). The high-resolution SEM image (Fig. 1b), however, shows that Ni foam is uniformly covered by Sn_3O_4 nanosheets with diameters ranging from 500 to 800 nm. Furthermore, as shown in Fig. 1c, the thickness of Sn_3O_x nanosheets is approximately 30–40 nm. The thickness of Sn_3O_x layer coating on the Ni foam is approximately 3.8 μm (Fig. 1d). Sn_3O_x was separately synthesized and exhibits a spherical structure composed of nanosheets agglomerated into micro flowers (Fig. S2). TEM results indicate that both the Sn_3O_4 (Fig. S3) and Sn_3O_x (Fig. 1e) have a nanosheet structure, which is consistent with SEM. High-resolution TEM (HRTEM) image (Fig. 1f) shows a crystalline lattice characteristic of Sn_3O_x. The lattice fringe spacing measured is approximately 0.35 nm, corresponding to the (101) plane of the triclinic structure of Sn_3O_x. Sn_3O_x structure becomes porous owing to ascorbic acid regulation. The pores are approximately 2 nm in size. Furthermore, an amorphous layer is formed on the surface of Sn_3O_x.

Based on the X-ray diffraction (XRD) results (Fig. 2a), the 2θ peak diffraction peak is identified at 44.5°, 51.8° and 76.4° corresponding to Ni (JCPDS No. 04-0850) (111), (200) and (220), respectively. The 2θ peak diffraction at 27.1°, 31.7°, 32.3°, 37.1°, 50.0°, 60.9° and 63.5° are consistent with Sn_3O_4 (JCPDS No. 16-0737) (111), ($\bar{2}$10), ($\bar{1}$21), (130), ($\bar{3}$01), (042) and (312), respectively. These findings strongly reveal that Sn_3O_4/Ni foam is successfully prepared, as no other impurity peaks are observed. The structure of the samples was investigated using Raman spectroscopy (Fig. 2b). Raman peaks of Sn_3O_4 at 70, 82, 136, 165 and 235 cm^{-1} can be seen in Sn_3O_4/Ni and Sn_3O_x/Ni foam photoanodes, indicating that Sn_3O_4 nanosheets have been successfully loaded onto the surface of Ni foam. Figure 2c shows the optical capabilities of the samples.

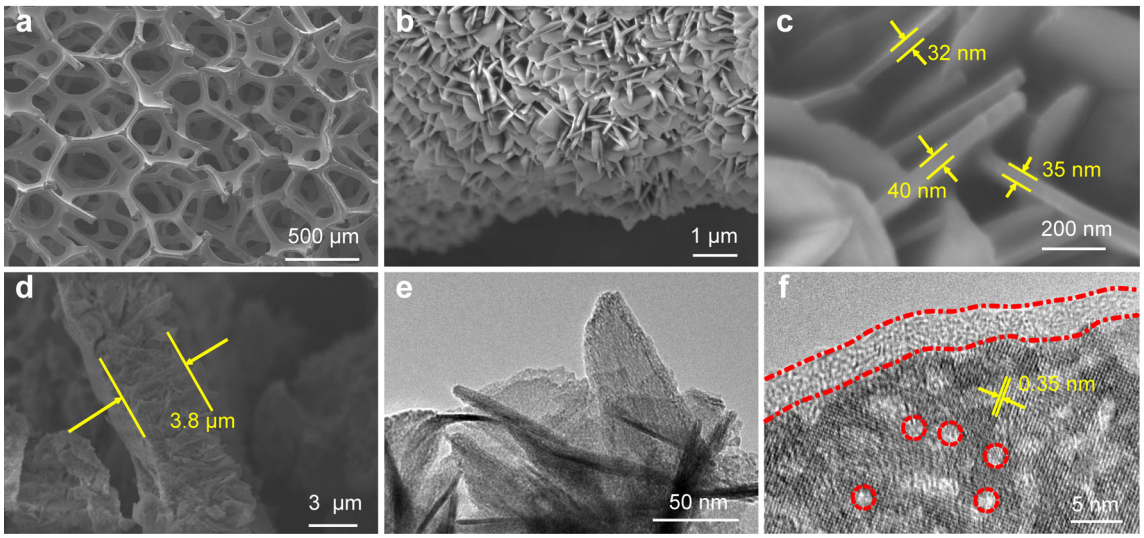

Fig. 1 **a, b** SEM images of Sn_3O_x nanosheet/Ni foam; **c, d** SEM images of surface amorphization oxygen vacancy-rich porous Sn_3O_x nanosheets on Ni foam; **e** TEM and **f** HRTEM images of surface amorphization oxygen vacancy-rich porous Sn_3O_x nanosheets on Ni foam

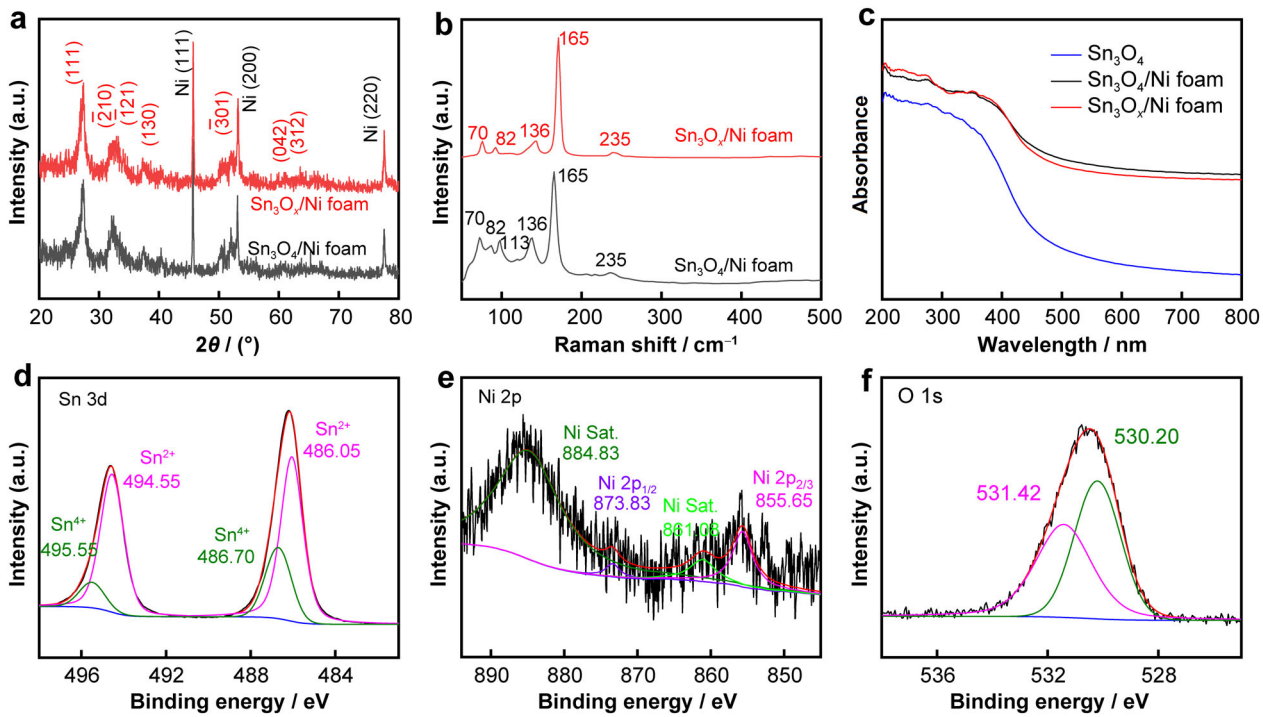

Fig. 2 **a** XRD patterns of Sn_3O_4/Ni foam and Sn_3O_x/Ni foam photoanode; **b** Raman spectra of Sn_3O_4/Ni foam and Sn_3O_x/Ni foam photoanode; **c** UV–Vis spectra of Sn_3O_4, Sn_3O_4/Ni foam and Sn_3O_x/Ni foam photoanode; high-resolution XPS spectra of **d** Sn 3d, **e** Ni 2p and **f** O 1s

Sn_3O_4 nanosheets spectrum is typical of wide bandgap oxide semiconductors, with an intense absorption band and steep cut-off at 440 nm. Sn_3O_4/Ni and Sn_3O_x/Ni foams absorb more light in the visible to near-infrared (NIR) spectral region than pure Sn_3O_4 nanosheets.

The surface chemical compositions and composing elements of these catalysts were then investigated using X-ray photoelectron spectroscopy (XPS). The broad-scan spectrum of Sn_3O_x/Ni foam photoanode is shown in Fig. S4; Sn 3d, Ni 2p and O 1s peaks are observed, confirming that the sample elements contain Sn, Ni and O. Sn 3d signals are decomposed into two characteristic peaks, Sn $3d_{3/2}$ and Sn $3d_{5/2}$, with components at 495.55 and 486.70 eV corresponding to Sn^{2+}, respectively, and

components near 494.55 and 486.05 eV corresponding to Sn^{4+}, respectively (Fig. 2d).

These findings confirm the presence of Sn^{2+} and Sn^{4+} in Sn_3O_x/Ni foam. The characteristic peaks in Ni 1s spectra of Sn_3O_x/Ni foam are attributed to Ni salt, Ni $2p_{2/3}$ and Ni $2p_{1/2}$ at 861.08, 855.65 and 873.83 eV, respectively (Fig. 2e). Furthermore, O 1s XPS profile could be fitted to two characteristic peaks. The 530.2 eV peak is caused by oxygen atoms bound to the metal, while the 531.4 eV peak is caused by defect sites with low oxygen coordination, indicating the presence of oxygen vacancies.

To evaluate PEC performance of Sn_3O_x/Ni foam photoanode, it is used to accelerate the processing of *E. coli* in water under light irradiation with a 0.8 V bias. When compared to Ni and Sn_3O_4/Ni foam photoanodes, the Sn_3O_x/Ni foam photoanode shows the highest *E. coli* inactivation performance (Fig. 3a). Figure 3b shows the direct *E. coli* inactivation properties by Sn_3O_x/Ni foam photoanode under different conditions. In the control group, the bacterial population remains unchanged after 40 min of exposed to Sn_3O_x/Ni foam photoanode. It has been demonstrated that Sn_3O_x/Ni foam photoanode is nontoxic to bacteria. However, under light irradiation or 0.8 V bias, approximately 1.7 and 2.2 log of *E. coli* was inactivated in 40 min. In contrast, *E. coli* is completely inactivated after 30 min of PEC treatment at 0.8 V bias and light irradiation. Reducing the bias potential of 0.2–0.8 V significantly increases the bacterial inactivation efficiency, indicating that the photocatalytic ability is positively related to the applied external bias (Fig. 3c).

Furthermore, to demonstrate the broad-spectrum bactericidal effect, we tested Gram-negative bacteria, Gram-positive bacteria, and drug-resistant bacteria (chloramphenicol-resistant *E. coli* (Chl^r *E. coli*) and methicillin-resistant *Staphylococcus aureus* (MRSA)), as shown in Fig. 3d, e. These findings demonstrate the universality of PEC oxidation in the treatment of various bacteria.

SEM was used to study the morphology of Chl^r *E. coli* before and after treatment to decipher the antibacterial behaviour. As shown in Fig. 3f, before treatment, Chl^r *E. coli* presented an intact cellular structure with a typical rod-like shape. Chl^r *E. coli* is severely misshapen and fractured after PEC oxidation, indicating that the generated ROS sabotage the bacterial cell wall. This result is also confirmed in the bacterial live/dead assay, distinguishing the live bacteria (stained in green) and dead bacteria (stained in red). As shown in Fig. 3f, initially, almost none of Chl^r *E. coli* are killed. Following PEC oxidation, all bacteria turned red, indicating mortality.

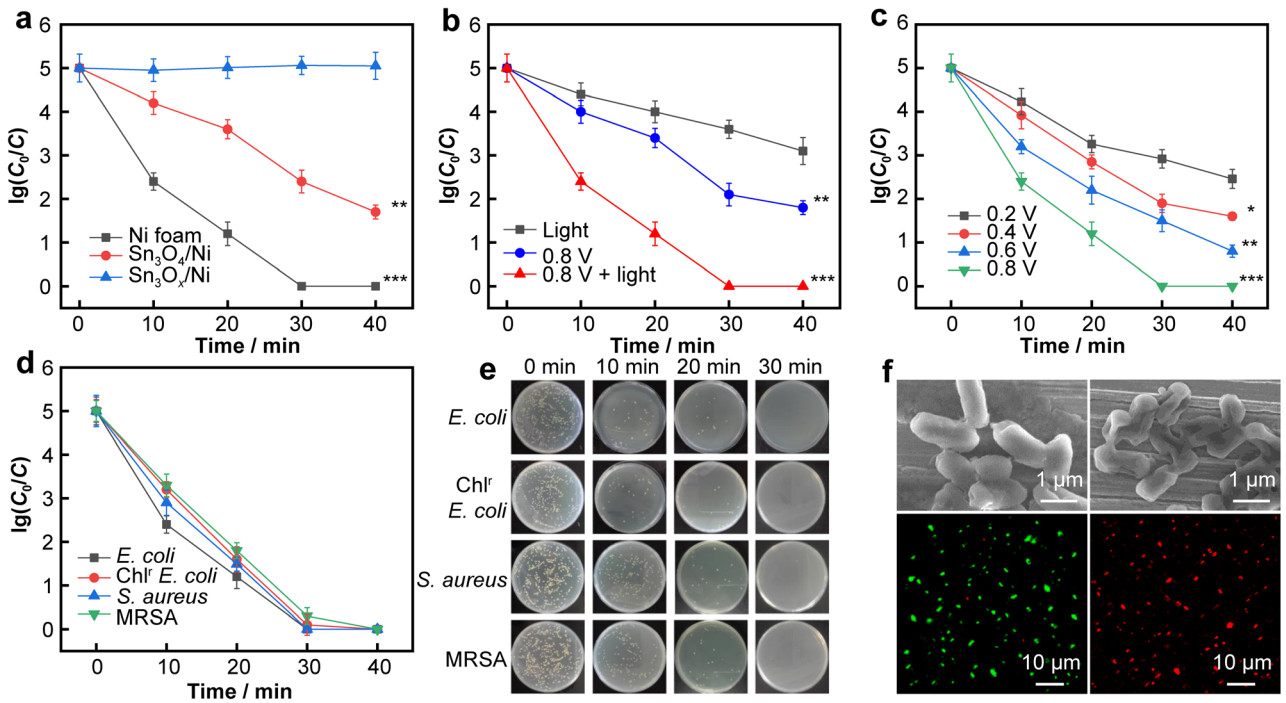

Fig. 3 *E. coli* inactivation under different conditions: **a** comparison of Ni foam, Sn_3O_4/Ni foam and Sn_3O_x/Ni foam; **b** comparison of light, 0.8 V bias and light + 0.8 V bias; **c** bias potential varying from 0.2 to 0.8 V, where $^*p < 0.05$, $^{**}p < 0.01$, $^{***}p < 0.001$ indicate significant differences compared to control group; **d** PEC inactivation of different bacteria (*E. coli*, Chl^r *E. coli*, *S. aureus* and MRSA); **e** corresponding photographs of bacterial colonies; **f** SEM images of Chl^r *E. coli* before and after PEC oxidation for 30 min, and corresponding fluorescence microscopic images (where *C* is terminal concentration of bacteria and C_0 is e concentration at $t = 0$ of experiments)

The photoelectric properties were tested to clarify the sterilization mechanism. In the dark, Sn_3O_4/Ni and Sn_3O_x/Ni foam photoanodes display extremely weak current densities, as shown in Fig. 4a. When the photoanodes are illuminated with light, an anodic photocurrent occurs, which increases as the bias potential increases. The flow of the photogenerated electrons through the outer circuit causes the photocurrent. As shown in Fig. 4b, Sn_3O_x/Ni foam photoanode demonstrates a significantly higher photocurrent than the Sn_3O_4/Ni foam photoanode, attributed to the improved charge separation and interfacial charge transfer in the photoanode. Furthermore, when the bias is varied (0.2, 0.4, 0.6 and 0.8 V), Sn_3O_x/Ni foam photoanode exhibits fast and reversible photocurrent responses for each on and off cycle and the photocurrent density increases as the bias voltages increase (Fig. S5).

According to the electrochemical impedance spectroscopy Nyquist analysis, the charge transfer resistance of electrodes, which is inversely proportional to the rate of charge transfer in the PEC process, can be calculated using the diameter of the fitted semi-circle [52, 53]. The obtained Nyquist plots of Sn_3O_4/Ni and Sn_3O_x/Ni foam photoanodes are shown in Fig. 4c. Nyquist plots of Sn_3O_4/Ni and Sn_3O_x/Ni foam photoanodes show semicircles. The low ohmic resistance of the as-fabricated photoanode suggests a fast charge transfer. Furthermore, the impedance is reduced further under light illumination, demonstrating that illumination promotes faster carrier transport on the surface. When compared to Sn_3O_4/Ni foam, the impedance of Sn_3O_x/Ni foam is reduced, indicating that the separation and transfer of photogenerated charges from Sn_3O_x/Ni foam yields the most efficient and fastest charge transfer performance that would improve PEC activities.

Furthermore, electron paramagnetic resonance (EPR) spectroscopy was carried out at 25 °C to demonstrate the formation of oxygen vacancies following ascorbic acid reduction. As shown in Fig. 4d, a single EPR signal associated with oxygen vacancies was observed in both Sn_3O_4 and Sn_3O_x. However, the signal of oxygen vacancies in Sn_3O_x is significantly higher than in Sn_3O_4, contributing to enhanced light absorption and the separation of photogenerated carriers.

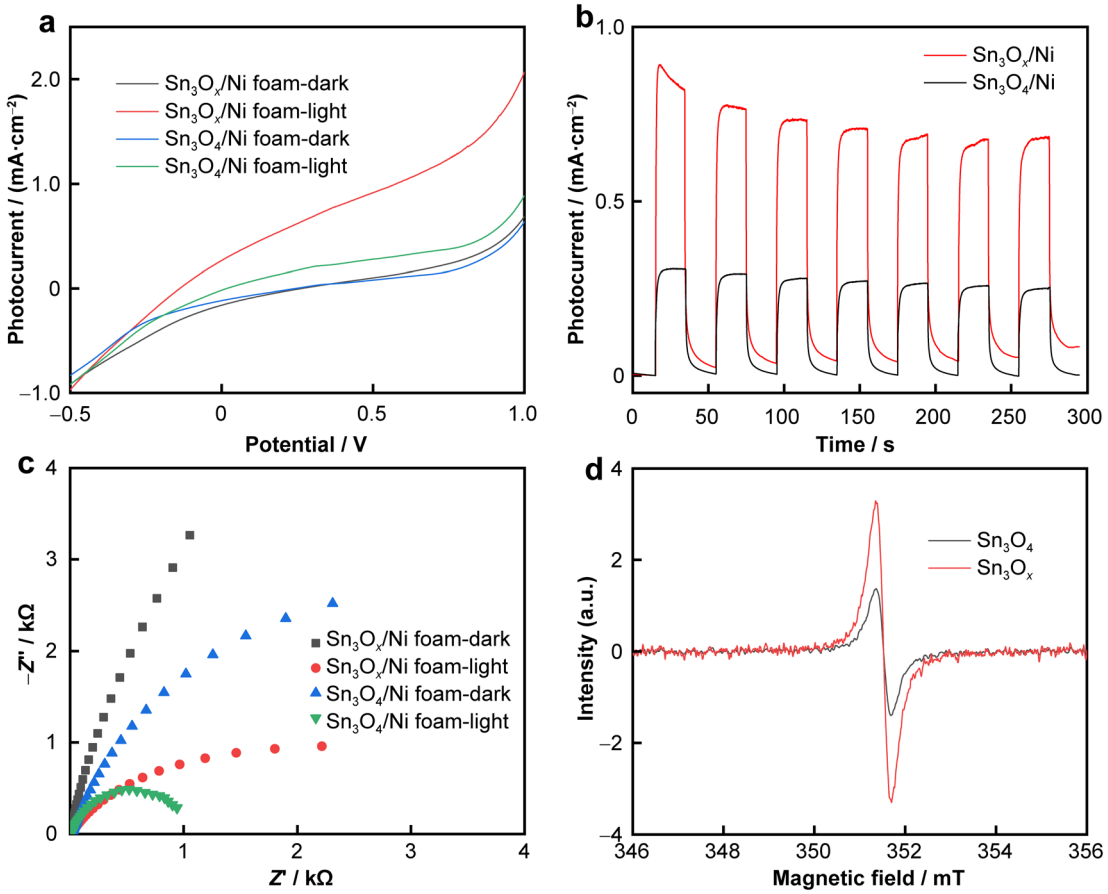

Fig. 4 **a** Current–voltage curves in dark and under light irradiation of Sn_3O_4/Ni foam and Sn_3O_x/Ni foam photoanodes; **b** photocurrent density ON–OFF curves of Sn_3O_4/Ni foam and Sn_3O_x/Ni foam photoanodes; **c** EIS Nyquist plots under dark and light irradiation of Sn_3O_4/Ni foam and Sn_3O_x/Ni foam (impedance is a complex number, Z' and Z'' represent real and imaginary parts, respectively); **d** EPR spectra of Sn_3O_4 and Sn_3O_x nanosheets

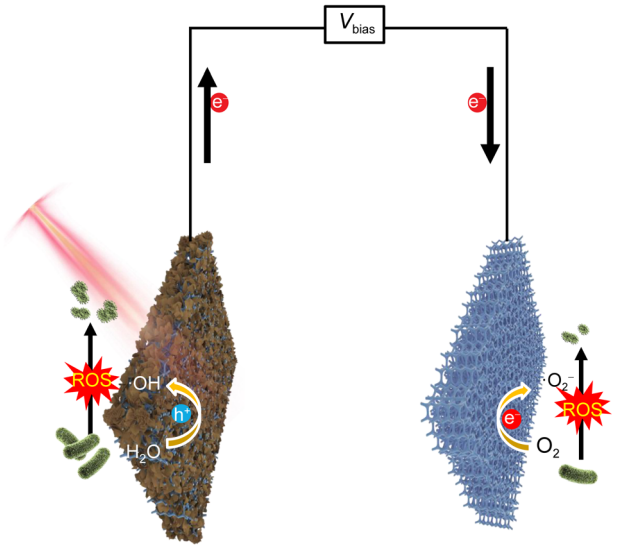

Fig. 5 Schematic illustration for Sn_3O_x/Ni foam photoanode

Based on the above experimental results, we propose a mechanism for PEC charge transfer and bacterial inactivation that occur on Sn_3O_x/Ni foam photoanode, as shown in Fig. 5. Sn_3O_x initially absorbs visible light to generate electron and hole pairs. The available wavelength range can be extended to the NIR region by forming a porous structure rich in oxygen vacancies. Under light irradiation, electron–hole pairs are formed, and the electron holes remain separated at the applied voltage and do not rapidly compound. On the photoanode, the generated holes from Sn_3O_x can react with H_2O to produce ·OH, which has the strongest oxidising ability of any ROS. Furthermore, $·O_2^-$ is produced on the cathode by electron reduction of O_2. Sn_3O_x/Ni foam has a porous structure, and the rough surfaces of the photoanode increase the contact area with bacteria. Further, the ROS produced directly acts on the bacteria, resulting in an excellent bactericidal effect.

3 Conclusion

To summarise, surface amorphisation oxygen vacancy-rich porous Sn_3O_x nanosheets in situ grown on Ni foam were successfully designed via a simple, one-step hydrothermal method, resulting in enhanced PEC activity for bacterial inactivation. PEC characterisation demonstrated an enhancement in photoelectric catalytic performance owing to a broadened absorption spectrum and effective separation of the electron–hole pairs. This outstanding photoelectrocatalyst demonstrated a 100% antibacterial effect in water against drug-resistant Gram-positive and Gram-negative bacteria. This surface amorphisation oxygen vacancy-rich porous Sn_3O_x nanosheet strategy can inspire the design and fabrication of other PEC systems for efficient photoelectrocatalytic bacterial inactivation.

Acknowledgements This study was financially supported by the National Natural Science Foundation of China (Nos. 51732007 and 52272212), the Natural Science Foundation of Shandong Province (No. ZR2022JQ20).

Declarations

Conflict of interests The authors declare that they have no conflict of interest.

References

[1] Alharthi S, Alavi SE, Moyle PM, Ziora ZM. Sortase A (SrtA) inhibitors as an alternative treatment for superbug infections. Drug Discov Today. 2021;26(9):2164. https://doi.org/10.1016/j.drudis.2021.03.019.

[2] Van Boeckel TP, Pires J, Silvester R, Zhao C, Song J, Criscuolo NG, Gilbert M, Bonhoeffer S, Laxminarayan R. Global trends in antimicrobial resistance in animals in low- and middle-income countries. Science. 2019;365(6549):1944. https://doi.org/10.1126/science.aaw1944.

[3] De Kraker MEA, Stewardson AJ, Harbarth S. Will 10 million people die a year due to antimicrobial resistance by 2050. PLoS Med. 2016;13(11):1002184. https://doi.org/10.1371/journal.pmed.1002184.

[4] Li XH, Fan H, Zi H, Hu HK, Li BH, Huang J, Luo PC, Zeng XT. Global and regional burden of bacterial antimicrobial resistance in urinary tract infections in 2019. J Clin Med. 2022;11(10):2817. https://doi.org/10.3390/jcm11102817.

[5] Luo XR, Zhang BP, Lu YH, Mei Y, Shen L. Advances in application of ultraviolet irradiation for biofilm control in water and wastewater infrastructure. J Hazard Mater. 2022;421(5):126682. https://doi.org/10.1016/j.jhazmat.2021.126682.

[6] Issaka E, Amu-Darko JNO, Yakubu S, Fapohunda FO, Ali N, Bilal M. Advanced catalytic ozonation for degradation of pharmaceutical pollutants-a review. Chemosphere. 2022;289:133208. https://doi.org/10.1016/j.chemosphere.2021.133208.

[7] Xing ZX, Cheng GJ, Yang H, Xue XX, Jiang PG. Mechanism and application of the ore with chlorination treatment: a review. Miner Eng. 2020;154:106404. https://doi.org/10.1016/j.mineng.2020.106404.

[8] Conejo AN, Birat JP, Dutta A. A review of the current environmental challenges of the steel industry and its value chain. J Environ Manage. 2020;259:109782. https://doi.org/10.1016/j.jenvman.2019.109782.

[9] Liu LY, Ji HG, Lu XF, Wang T, Zhi S, Pei F, Quan DL. Mitigation of greenhouse gases released from mining activities: a review. Int J Miner Metall Mater. 2021;28:513. https://doi.org/10.1007/s12613-020-2155-4.

[10] Tauseef SM, Abbasi T, Abbasi SA. Energy recovery from wastewaters with high-rate anaerobic digesters. Renew Sustain Energy Rev. 2013;19:704. https://doi.org/10.1016/j.rser.2012.11.056.

[11] Lv R, Liang YQ, Li ZY, Zhu SL, Cui ZD, Wu SL. Flower-like CuS/graphene oxide with photothermal and enhanced photocatalytic effect for rapid bacteria-killing using visible light. Rare Met. 2022;41(2):639. https://doi.org/10.1007/s12598-021-01759-4.

[12] Waso M, Reyneke B, Havenga B, Khan S, Khan W. Insights into Bdellovibrio spp. mechanisms of action and potential

applications. World J Microbiol Biotechnol. 2021;37:85. https://doi.org/10.1007/s11274-021-03054-x.
[13] Wang LW, Gao FE, Wang AZ, Chen XY, Li H, Zhang X, Zheng H, Ji R, Li B, Yu X, Liu J, Gu ZJ, Chen FL, Chen CY. Defect-rich adhesive molybdenum disulfide/rGO vertical heterostructures with enhanced nanozyme activity for smart bacterial killing application. Adv Mater. 2020;32(48):2005423. https://doi.org/10.1002/adma.202005423.
[14] Wang ZM, Shen ZY, Li YM, Zuo JL. Preparation and photoelectrocatalytic performance of Ru loaded TiO_2 nanotubes. Chin J Rare Met. 2020;44(6):609. https://doi.org/10.13373/j.cnki.cjrm.XY18120018.
[15] Wang LW, Zhang X, Yu X, Gao FE, Shen ZY, Zhang XL, Ge SG, Liu J, Gu ZJ, Chen CY. An all-organic semiconductor C_3N_4/PDINH heterostructure with advanced antibacterial photocatalytic therapy activity. Adv Mater. 2019;31(33):1901965. https://doi.org/10.1002/adma.201901965.
[16] Ferraz NP, Nogueira AE, Marcos FCF, Machado VA, Rocca RR, Assaf EM, Asencios YJO. CeO_2–Nb_2O_5 photocatalysts for degradation of organic pollutants in water. Rare Met. 2020;39(3):230. https://doi.org/10.1007/s12598-019-01282-7.
[17] Huang G, Xu ZH, Luo TT, Yan ZX, Zhang M. Fluorescent light enhanced graphitic carbon nitride/ceria with ultralow-content platinum catalyst for oxidative decomposition of formaldehyde at ambient temperature. Rare Met. 2021;40(11):3135. https://doi.org/10.1007/s12598-021-01756-7.
[18] Zhao Y, Liu J, Han M, Yang G, Ma L, Wang Y. Two comparable Ba-MOFs with similar linkers for enhanced CO_2 capture and separation by introducing N-rich groups. Rare Met. 2021;40(2):499. https://doi.org/10.1007/s12598-020-01597-w.
[19] Yang RQ, Song GX, Wang LW, Yang ZW, Zhang J, Zhang X, Wang S, Ding LH, Ren N, Wang AZ, Yu X. Full solar-spectrum-driven antibacterial therapy over hierarchical Sn_3O_4/PDINH with enhanced photocatalytic activity. Small. 2021;17(39):2102744. https://doi.org/10.1002/smll.202102744.
[20] Zhou Z, Li B, Liu X, Li Z, Zhu S, Liang Y, Cui Z, Wu S. Recent progress in photocatalytic antibacterial. ACS Appl Bio Mater. 2021;4:3909. https://doi.org/10.1021/acsabm.0c01335.
[21] Li PP, Wu HX, Dong A. Ag/AgX nanostructures serving as antibacterial agents: achievements and challenges. Rare Met. 2022;41(2):519. https://doi.org/10.1007/s12598-021-01822-0.
[22] Zeng JY, Li ZM, Jiang H, Wang XM. Progress on photocatalytic semiconductor hybrids for bacterial inactivation. Mater Horiz. 2021;8:2964. https://doi.org/10.1039/D1MH00773D.
[23] Yu X, Jin X, Chen XY, Wang AZ, Zhang JM, Zhang J, Zhao ZH, Gao MM, Razzari L, Liu H. A microorganism bred TiO_2/Au/TiO_2 heterostructure for whispering gallery mode resonance assisted plasmonic photocatalysis. ACS Nano. 2020;14(10):13876. https://doi.org/10.1021/acsnano.0c06278.
[24] Li JF, Li ZY, Liu XM, Li CY, Zheng YF, Yeung KWK, Cui ZD, Liang YQ, Zhu SL, Hu WB, Qi YJ, Zhang TJ, Wang XB, Wu SL. Interfacial engineering of Bi_2S_3/$Ti_3C_2T_x$ MXene based on work function for rapid photo-excited bacteria-killing. Nat Commun. 2021;12:1. https://doi.org/10.1038/s41467-021-21435-6.
[25] Guo H, Li J, Zou XR, Wang HS, Kang A, Zhou H, Li MJ, Zhao XY. Fabrication of GO-TiO_2/(Ca, Y)F-2:Tm, Yb composites with high-efficiency optical driving photocatalytic activity for degradation of organic dyes and bacteriostasis. Rare Met. 2022;41(2):650. https://doi.org/10.1007/s12598-021-01831-z.
[26] Li JY, Ma AQ, Li HF, Dong YH, Gao YQ. Tunable micromorphology and photocatalytic properties of monoclinic $BiVO_4$ prepared by bionic template method. Chin J Rare Met. 2020;44(9):912. https://doi.org/10.13373/j.cnki.cjrm.xy19060008.
[27] Zhang P, Yu L, Lou XW. Construction of heterostructured Fe_2O_3-TiO_2 microdumbbells for photoelectrochemical water oxidation. Angew Chem Int Ed. 2018;57:15076. https://doi.org/10.1002/anie.201808104.
[28] Ji YC, Yang RQ, Wang LW, Song GX, Wang AZ, Lv YW, Gao MM, Zhang J, Yu X. Visible light active and noble metal free Nb_4N_5/TiO_2 nanobelt surface heterostructure for plasmonic enhanced solar water splitting. Chem Eng J. 2020;402: 126226. https://doi.org/10.1016/j.cej.2020.126226.
[29] Sun JY, Wen JH, Wu GZ, Zhang Z, Chen X, Wang GC, Liu MY. Harmonizing the electronic structures on BiOI with active oxygen vacancies toward facet-dependent antibacterial photodynamic therapy. Adv Func Mater. 2020;30(42):2004108. https://doi.org/10.1002/adfm.202004108.
[30] Vorobyova V, Vasyliev G, Uschapovskiy D, Lyudmyla K, Skiba M. Green synthesis, characterization of silver nanoparticals for biomedical application and environmental remediation. J Microbiol Methods. 2022;193:106384. https://doi.org/10.1016/j.mimet.2021.106384.
[31] Fu JN, Zhu WD, Liu XM, Liang CY, Zheng YF, Li ZY, Liang YQ, Zheng D, Zhu SL, Cui ZD, Wu SL. Self-activating anti-infection implant. Nature Commun. 2021;12:1. https://doi.org/10.1038/s41467-021-27217-4.
[32] Feng YJ, Wang Y, Wang KW, Ma JP, Duan YY, Liu J, Lu X, Zhang B, Wang GY, Zhou XY. Ultra-fine Cu clusters decorated hydrangea-like titanium dioxide for photocatalytic hydrogen production. Rare Met. 2022;41(2):385. https://doi.org/10.1007/s12598-021-01815-z.
[33] Yu X, Zhao ZH, Sun DH, Ren N, Ding LH, Yang RQ, Ji YC, Li LL, Liu H. TiO_2/TiN core/shell nanobelts for efficient solar hydrogen generation. Chem Commun. 2018;54(47):6056. https://doi.org/10.1039/C8CC02651C.
[34] Wang WC, Zhu S, Cao YN, Tao Y, Li X, Pan DL, Phillips DL, Zhang DQ, Chen M, Li GS, Li HX. Edge-enriched ultrathin MoS_2 embedded yolk-shell TiO_2 with boosted charge transfer for superior photocatalytic H_2 evolution. Adv Func Mater. 2019;29(36):1901958. https://doi.org/10.1002/adfm.201901958.
[35] Chen WJ, Li SY, Wang J, Sun K, Si YB. Metal and metal-oxide nanozymes: bioenzymatic characteristics, catalytic mechanism, and eco-environmental applications. Nanoscale. 2019;11:15783. https://doi.org/10.1039/C9NR04771A.
[36] Li XM, Wu DH, Hua T, Lan XQ, Han SP, Cheng JH, Du KS, Hu YY, Chen YC. Micro/macrostructure and multicomponent design of catalysts by MOF-derived strategy: opportunities for the application of nanomaterials-based advanced oxidation processes in wastewater treatment. Sci Total Environ. 2022;804:150096. https://doi.org/10.1016/j.scitotenv.2021.150096.
[37] Soares SF, Fernandes T, Trindade T, Daniel-da-Silva AL. Recent advances on magnetic biosorbents and their applications for water treatment. Environ Chem Lett. 2020;18:151. https://doi.org/10.1007/s10311-019-00931-8.
[38] Wang RQ, Wang FK, Zhang X, Feng X, Zhao CD, Bu KJ, Zhang Z, Zhai TY, Huang FQ. Improved polarization in the $Sr_6Cd_2Sb_6O_7Se_{10}$ oxyselenide through design of lateral sublattices for efficient photoelectric conversion. Angew Chem Int Ed. 2022;61(33):e202206816. https://doi.org/10.1002/ange.202206816.
[39] Zheng XL, Wu DX, Liu YH, Li J, Yang YJ, Huang W, Liu WF, Shen YJ, Tian XL. Photocatalytic reduction of water to hydrogen by $CuPbSbS_3$ nanoflakes. Mater Today Energy. 2022;25:100956. https://doi.org/10.1016/j.mtener.2022.100956.
[40] Liu ZR, Wang LW, Yu X, Zhang J, Yang RQ, Zhang XD, Ji YC, Wu MQ, Deng L, Li LL, Wang ZL. Piezoelectric-effect-enhanced full-spectrum photoelectrocatalysis in p–n heterojunction. Adv Func Mater. 2019;29(41):1807279. https://doi.org/10.1002/adfm.201807279.
[41] Yang RQ, Ji YC, Wang LW, Song GX, Wang AZ, Ding LH, Ren N, Lv YW, Zhang J, Yu X. Crystalline Ni-doped Sn_3O_4

nanosheets for photocatalytic H_2 production. ACS Appl Nano Mater. 2020;3:9268. https://doi.org/10.1021/acsanm.0c01886.
[42] Cho YU, Lee JY, Jeong UJ, Park S, Lim SL, Kim KY, Jang JW, Park JH, Kim HW, Shin H, Jeon H, Jung YM, Cho IJ, Yu KJ. Ultra-low cost, facile fabrication of transparent neural electrode array for electrocorticography with photoelectric artifact-free optogenetics. Adv Funct Mater. 2022;32(10):2105568. https://doi.org/10.1002/adfm.202105568.
[43] Zheng XL, Yang YJ, Liu YH, Deng PL, Li J, Liu WF, Rao P, Jia CM, Huang W, Du YL, Shen YJ, Tian XL. Fundamentals and photocatalytic hydrogen evolution applications of quaternary chalcogenide semiconductor: Cu_2ZnSnS_4. Rare Met. 2022;41(7):2153. https://doi.org/10.1007/s12598-021-01955-2.
[44] Wan ST, Li HT, Ma ZH, Zhang HC, Zheng YZ. 2D/2D heterostructured $MoS_2/PtSe_2$ promoting charge separation in FTO thin film for efficient and stable photocatalytic hydrogen evolution. Rare Met. 2022;41(5):1735. https://doi.org/10.1007/s12598-021-01954-3.
[45] Zhang M, Xuan XX, Wang WL, Ma CY, Lin ZQ. Anode photovoltage compensation-enabled synergistic CO_2 photoelectrocatalytic reduction on a flower-like graphene-decorated Cu foam cathode. Adv Funct Mater. 2020;30(52):2005983. https://doi.org/10.1002/adfm.202005983.
[46] Yang RQ, Ji YC, Li Q, Zhao ZH, Zhang RT, Liang LL, Liu F, Chen YK, Han SW, Yu X, Liu H. Ultrafine Si nanowires/Sn_3O_4 nanosheets 3D hierarchical heterostructured array as a photoanode with high-efficient photoelectrocatalytic performance. Appl Catal B. 2019;256:117798. https://doi.org/10.1016/j.apcatb.2019.117798.
[47] Zhang G, Zhang ZH, Xia DH, Qu Y, Wang WQ. Solar driven self-sustainable photoelectrochemical bacteria inactivation in scale-up reactor utilizing larg-scale fabricable Ti/MoS_2/MoO_x photoanode. J Hazard Mater. 2020;392: 122292. https://doi.org/10.1016/j.jhazmat.2020.122292.
[48] Zhu LP, Lu H, Hao D, Wang LL, Wu ZH, Wang LJ, Li P, Ye JH. Three-dimensional lupinus-like TiO_2 nanorod@Sn_3O_4 nanosheet hierarchical heterostructured arrays as photoanode for enhanced photoelectrochemical performance. ACS Appl Mater Interfaces. 2017;9:38537. https://doi.org/10.1021/acsami.7b11872.
[49] Balgude S, Sethi Y, Kale B, Amalnerkar D, Adhyapak P. Sn_3O_4 microballs as highly efficient photocatalyst for hydrogen generation and degradation of phenol under solar light irradiation. Mater Chem Phys. 2019;221:493. https://doi.org/10.1016/j.matchemphys.2018.08.032.
[50] Li CM, Yu SY, Dong HJ, Liu CB, Wu HJ, Che HN, Chen G. Z-scheme mesoporous photocatalyst constructed by modification of Sn_3O_4 nanoclusters on g-C_3N_4 nanosheets with improved photocatalytic performance and mechanism insight. Appl Catal B. 2018;238:284. https://doi.org/10.1016/j.apcatb.2018.07.049.
[51] Yang RQ, Ji YC, Zhang J, Zhang RT, Liu F, Chen YK, Liang LL, Han SW, Yu X, Liu H. Efficiently degradation of polyacrylamide pollution using a full spectrum Sn_3O_4 nanosheet/Ni foam heterostructure photoelectrocatalyst. Catal Today. 2019;335:520. https://doi.org/10.1016/j.cattod.2019.02.019.
[52] Yang RQ, Liang N, Chen XY, Wang LW, Song GX, Ji YC, Ren N, Lv YW, Zhang J, Yu X. Sn/Sn_3O_{4-x} heterostructure rich in oxygen vacancies with enhanced visible light photocatalytic oxidation performance. Int J Miner Metall Mater. 2021;28(1):150. https://doi.org/10.1007/s12613-020-2131-z.
[53] Yu X, Zhao ZH, Zhang J, Guo WB, Qiu JC, Li DS, Li Z, Mou XN, Li LL, Li AX. Rutile nanorod/anatase nanowire junction array as both sensor and power supplier for high-performance, self-powered, wireless UV photodetector. Small. 2016;12:2759. https://doi.org/10.1002/smll.201503388.

Springer Nature or its licensor (e.g. a society or other partner) holds exclusive rights to this article under a publishing agreement with the author(s) or other rightsholder(s); author self-archiving of the accepted manuscript version of this article is solely governed by the terms of such publishing agreement and applicable law.